

The Kratos Framework for Heterogeneous Astrophysical Simulations: Ray Tracing, Reacting Flow and Thermochemistry

LILE WANG^{1,2}

¹ *The Kavli Institute for Astronomy and Astrophysics, Peking University, Beijing 100871, China*

² *Department of Astronomy, School of Physics, Peking University, Beijing 100871, China*

ABSTRACT

Thermochemistry, ray-tracing, and radiation-matter interactions are important processes which are computationally difficult to model in astrophysical simulations, addressed by introducing novel algorithms optimized for heterogeneous architectures in the Kratos framework. Key innovations include a stoichiometry-compatible reconstruction scheme for consistent chemical species advection, which ensures element conservation while avoiding matrix inversions, and a LU decomposition method specifically designed for multi-thread parallelization in order to solve stiff thermochemical ordinary differential equations with high efficiency. The framework also implements efficient ray-tracing techniques for radiation-matter interactions. Various verification tests, spanning from chemical advection, combustion, Strömgren spheres, and detonation dynamics, are conducted to demonstrate the accuracy and robustness of Kratos, with results closely matching semi-analytic solutions and benchmarks such as Cantera and the Shock and Detonation Toolbox. The modular design and performance optimizations position it as a versatile tool for studying coupled microphysical processes in the diverse environments of contemporary astrophysical studies.

Keywords: Astronomy software (1855), Computational methods (1965), GPU computing (1969), Chemical reaction network models (2237), Hydrodynamical simulations (767)

1. INTRODUCTION

Astrophysical reacting flows are among the most complex and fascinating phenomena in the universe, involving a wide range of physical processes such as hydrodynamics, magnetohydrodynamics (MHD), thermochemistry, and radiation. These processes are intricately coupled and play crucial roles in various astrophysical phenomena, including planet formation, star formation, stellar evolution, supernova explosions, and the formation of galaxies. To gain a deeper understanding of these phenomena, numerical simulations have become an essential tool, allowing researchers to model and analyze the underlying mechanisms in detail.

Consistent microphysics calculations, including thermochemistry and radiation, are emerging as necessities for numerical simulations of astrophysical processes (e.g. [Zingale et al. 2024](#)). Thermochemistry, in particular,

is a critical component that governs the chemical reactions and energy release in astrophysical environments. However, thermochemical calculations are often computationally expensive due to the stiffness of the thermochemical systems, which makes them challenging to integrate into dynamic simulations. As a result, most previous works have either focused on static grids or neglected the consistency between fluid mechanics and thermochemistry. This limitation has hindered the development of comprehensive models that can accurately capture the full complexity of astrophysical reacting flows.

Existing computational codes that claim to be at the forefront of research often face several challenges. First, many codes have restricted availability or are subject to copyright limitations, which restricts their widespread use and collaboration opportunities. Second, some codes lack the capability to efficiently integrate with hydrodynamic calculations, often due to the computational inefficiencies associated with thermochemical calculations. Finally, the reliability and accuracy of these codes are not always well-controlled, which can lead to uncertainties in the simulation results.

Corresponding author: Lile Wang
 lilew@pku.edu.cn

To address these challenges, the Kratos code based on heterogeneous devices, especially GPUs (graphical processing units), aims to provide a comprehensive and efficient solution for simulating astrophysical reacting flows. By integrating consistent microphysics calculations with hydrodynamics, the system seeks to overcome the limitations of previous approaches and enable more accurate and reliable simulations of astrophysical phenomena. This work is expected to contribute significantly to the field by providing a powerful tool for researchers to explore the complex interactions between different physical processes in astrophysical environments. The method described in this paper has actually been adopted in several astrophysical works already. An earlier version of the GPU-based thermochemistry module developed by the author, although based on the hydrodynamics and MHD of Athena++ (Stone et al. 2020), have been applied in various astrophysical scenarios, including protoplanetary disk photoevaporation (Wang & Goodman 2017) and magnetized disk winds (Wang et al. 2019; Hu et al. 2019; Nemer et al. 2020; Fang et al. 2023), exoplanetary atmospheres (Wang & Dai 2018, 2019, 2021a,b), and interstellar media (Yue et al. 2024). Implementing the microphysics modules on Kratos, a platform with optimized algorithms and procedures intrinsically designed for GPUs, offers a high-performance platform including co-evolved with real-time microphysics, which are crucial to various incoming comprehensive simulations that aim at the consistency of astrophysical processes studies.

This paper is structured as follows. §2 elaborates the methods for thermochemistry specifically adapted for GPUs, focusing on the conservation laws and the parallelization of algorithms. §3 describes the GPU-optimized ray tracing method, including the geometric calculations on the structured mesh of Kratos and the details of radiation-materials interactions based on the structured mesh. §4 exhibits verifications and tests regarding the microphysics modules, including thermochemistry alone, radiation alone, and the tests that comprehensively involve the interactions of fluids, chemicals, and radiation. The implementation and results of these methods are summarized in §5, along with discussion about prospective future improvements.

2. THERMOCHEMISTRY AND REACTING FLOWS

The reacting flow module elaborated in this paper is part of Kratos, a grid-based heterogeneous system for astrophysical simulations (Wang 2025a). The flexibility of the Kratos framework and its hydrodynamic module allows straightforward implementations of consistent advection schemes for chemical species (§2.1), which is the

foundation of all procedures for reacting flow computations. Similar to the hydrodynamics module described in (Wang 2025a), the thermochemistry module also has three modes in terms of floating point precision, including a full single-precision mode, a full double-precision mode, and a mixed-precision mode that use double-precision operations only when updating the conserved quantities (the final abundance of chemical species at the end of each thermochemistry cycle). It is noted that Kratos allows the user to select the subset of chemical species and reactions involved, simply by assigning the list of the chemical species and the file of reaction database in the input file.

2.1. Conservation of Chemicals in Fluid Advection

A wide range of applications within the Kratos framework, including all computations discussed in this work, rely on the higher order schemes for reconstruction (e.g., piecewise linear method; PLM) and a Riemann solver (e.g., HLLC) for hydrodynamic fluxes. This combination achieves a balance between computational efficiency and numerical accuracy, making it suitable for simulating complex astrophysical reacting flows. In this section, we focus on the advection of chemical species, which is a critical component of the framework, as it ensures the conservation of chemical elements while maintaining numerical stability.

The advection scheme in Kratos is implemented as a Godunov solver, which consists of three primary steps: (1) reconstruction of variable values at cell interfaces, (2) calculation of fluxes using a Riemann solver, and (3) updating variables by adding the divergence of fluxes. Conservation of chemical elements is inherently guaranteed in the third step, provided that the first two steps are implemented correctly. This is particularly important in astrophysical simulations, where strict conservation of chemical abundances is required unless nuclear reactions are explicitly involved. To illustrate the methodology, a one-dimensional problems is considered, though the schemes can be straightforwardly extended to three dimensions. The flux of the s th chemical species at the $i - 1/2$ surface (left surface of the i th cell) is given by:

$$\mathcal{F}_{i-1/2}^s = x_{i-1/2}^s \mathcal{F}_{i-1/2}^\rho ; \quad x_{i-1/2}^s \equiv \left[\frac{n^s}{\rho} \right]_{i-1/2} , \quad (1)$$

where $[n^s/\rho]_{i-1/2}$ represents the ratio of the number density of the s th species to the mass density at the $i - 1/2$ surface. Here, $F_{i-1/2}^s$ and $\mathcal{F}_{i-1/2}^\rho$ denote the fluxes of the s th species in terms of molecule numbers and mass density, respectively. This formulation ensures that the advection of chemical species is consistent with the underlying hydrodynamics, thereby preserving

the integrity of chemical element abundances throughout the simulation domain.

It is straightforward to formulate the element conservation condition for chemical species fluxes at cell interfaces. For each element indexed by ν , the conservation relationship can be expressed as:

$$\sum_s \mathcal{N}_{\nu,s} \mathcal{F}_{i-1/2}^s = \frac{1}{\alpha} X_\nu \mathcal{F}_{i-1/2}^\rho, \quad (2)$$

where s iterates over all chemical species, $\mathcal{N}_{\nu,s}$ denotes the number of atoms of the ν^{th} element in the s^{th} species, X_ν represents the relative nuclear abundance of the ν^{th} element, and $\alpha \equiv \sum_\nu X_\nu m_\nu$ defines the mean *atomic* mass. Eq. (2) constitutes an underdetermined system when the number of species exceeds the number of elements. This conservation condition remains mathematically well-posed only under the assumption of constant elemental abundances, formally expressed as,

$$\sum_s \mathcal{N}_{\nu,s} n_i^s = \frac{1}{\alpha} X_\nu \rho_i, \quad \forall i. \quad (3)$$

A critical examination reveals that directly employing absolute or relative abundances in numerical schemes while allowing independent reconstruction and Riemann solver for individual species proves fundamentally flawed. This approach fails because higher-order reconstruction methods (e.g., piecewise linear methods) employ nonlinear transformations during interface value reconstruction. Consequently, the element conservation requirement stipulated by eq. (2) becomes systematically violated in such implementations. The nonlinear nature of these reconstruction operators disrupts the linear proportionality between species fluxes and density fluxes that element conservation demands.

2.1.1. Consistent Multifluid Advection (CMA)

To maintain accurate elemental abundances in multispecies fluid simulations, the concept of Consistent Multifluid Advection (CMA) was pioneered by Plewa & Müller (1999) and significantly advanced by Glover et al. (2010). Although possible if users desire, it is emphasized that CMA is *not* included in Kratos by default, and the following descriptions are presented only for logical completeness.

The CMA approach modifies the reconstructed relative species abundances $\{\tilde{x}_{i-1/2}^s\}$ through element conservation constraints. The corrected interface abundances $\{x_{i-1/2}^s\}$ are computed via:

$$x_{i-1/2}^s = \sum_\nu \frac{\mathcal{N}_{\nu,s}}{\mathcal{N}_{\text{tot},s}} \eta_\nu \tilde{x}_{i-1/2}^s, \quad (4)$$

where $\mathcal{N}_{\text{tot},s} \equiv \sum_\nu \mathcal{N}_{\nu,s}$ denotes the total nuclei count per molecule of species s . The correction coefficients $\{\eta_\nu\}$ are determined by solving the linear system:

$$\begin{aligned} \sum_s \mathcal{N}_{\mu,s} x_{i-1/2}^s &\equiv \sum_\nu \mathcal{M}_{\mu,\nu} \eta_\nu = \frac{X_\mu}{\alpha}, \\ \mathcal{M}_{\mu,\nu} &\equiv \sum_s \mathcal{N}_{\mu,s} \frac{\mathcal{N}_{\nu,s}}{\mathcal{N}_{\text{tot},s}} \tilde{x}_{i-1/2}^s, \end{aligned} \quad (5)$$

where $\mathcal{M}_{\mu,\nu}$ constitutes an element coupling matrix. This $O(N_{\text{elem}})$ linear system requires independent solution at each cell interface ($i - 1/2$), whose computational costs are expensive at the order of $O(N_{\text{elem}}^3)$. More crucially, the modified reconstruction $\{x_{i-1/2}^s\}$ preserves the spatial accuracy order of the original scheme applied to $\{\tilde{x}_{i-1/2}^s\}$.

2.1.2. Donor-cell Reconstruction: Conserved, but Lowest Order

A physically intuitive approach to determining $\{x_{i-1/2}^s\}$ emerges from Riemann solver behavior. The Riemann solvers naturally capture contact discontinuities where no species mixing occurs across wave surfaces—a property enforced by the Courant-Friedrichs-Lowy (CFL) condition. This implies that the relative species abundance at cell interfaces should inherit values from the upwind cell, determined by the contact surface's motion direction. This motivates a donor-cell-type scheme formulated as:

$$x_{i-1/2}^s = \left(\frac{n_{i-1}^s}{\rho_{i-1}} \right) \Theta(\mathcal{F}_{i-1/2}^\rho) + \left(\frac{n_i^s}{\rho_i} \right) \Theta(-\mathcal{F}_{i-1/2}^\rho), \quad (6)$$

where $\Theta(x)$ represents the Heaviside step function (0 if $x \leq 0$ and 1 otherwise).

Under the global element abundance constraint (eq. 3), this formulation inherently satisfies the flux conservation condition in eq. (2). Key advantages of this scheme include the minimal computational overhead through direct upwind selection, and the compatibility with spatially varying element abundances (unlike the CMA method). Nonetheless, significant diffusivity stems from strict proportionality between species fluxes and the upwind values (eq. 1), which remains as an apparent issue to be resolved.

2.1.3. Stoichiometry-compatible Reconstruction: Matrix Inversion Avoided for Higher Order

To match the contemporary reconstruction methods with higher spatial order of accuracy, an alternative higher-order scheme is implemented in Kratos, which avoids computational bottlenecks associated with matrix inversion in CMA while surpassing the spatial accuracy of donor-cell methods. Central to this approach

is the stoichiometric space \mathcal{S} , defined as the null space of the element-species matrix $\mathcal{N}_{\nu,s}$. By construction, any variation $\Delta n^s \in \mathcal{S}$ preserves elemental abundances,

$$n^s \rightarrow (n^s + \Delta n^s) \text{ , with } \sum_s \mathcal{N}_{\nu,s} \Delta n^s = 0 \text{ , } \forall \nu . \quad (7)$$

Let \mathcal{P} denote the projection operator associated with $\mathcal{N}_{\nu,s}$, which can be constructed during initialization through singular value decomposition (SVD) of the stoichiometric matrix,

$$\mathcal{N}_{\nu,s} = \mathbf{U} \Sigma \mathbf{V}^\top \Rightarrow \mathcal{P} = \mathbf{V} \mathbf{V}^\top , \quad (8)$$

where \mathbf{V} and \mathbf{U} contains the right and left singular vectors spanning the right and left spaces of \mathcal{S} , and Σ is the diagonal matrix for singular values. The SVD procedure are included in Kratos, which typically accounts for a negligible fraction of total runtime in practical simulations, as it only needs to be conducted once at the beginning of each run.

The interface states can be expressed through generalized reconstruction:

$$\begin{aligned} x_{i-1/2,l}^s &= \langle x \rangle_{i-1}^s + \chi_{i-1/2,l}^s \\ x_{i-1/2,r}^s &= \langle x \rangle_i^s + \chi_{i-1/2,r}^s \end{aligned} \quad (9)$$

where $\chi_{i-1/2,l/r}^s$ contains higher-order correction terms. For instance, in the piecewise linear method (PLM) reconstruction scheme adopted in Kratos by default, these terms take the form,

$$\begin{aligned} \chi_{i-1/2,l}^s &= \phi \left(\partial x_{i-1,f}^s, \partial x_{i-1,b}^s, c_{i-1,f}, c_{i-1,b} \right) \\ &\quad \times (\xi_{i-1/2} - \langle \xi \rangle_{i-1}) \\ \chi_{i-1/2,r}^s &= \phi \left(\partial x_{i,f}^s, \partial x_{i,b}^s, c_{i,f}, c_{i,b} \right) \\ &\quad \times (\xi_{i-1/2} - \langle \xi \rangle_i) , \end{aligned} \quad (10)$$

where ξ denotes spatial coordinate, $\xi_{i-1/2}$ the interface position, and $\langle \xi \rangle_i$ the cell-centered coordinate. The gradient terms and geometric coefficients are defined as,

$$\begin{aligned} \partial x_{i-1,f}^s &\equiv \frac{\langle x \rangle_i^s - \langle x \rangle_{i-1}^s}{\langle \xi \rangle_i - \langle \xi \rangle_{i-1}}, \quad \partial x_{i-1,b}^s \equiv \frac{\langle x \rangle_{i-1}^s - \langle x \rangle_{i-2}^s}{\langle \xi \rangle_{i-1} - \langle \xi \rangle_{i-2}} ; \\ c_{i-1,f} &\equiv \frac{\langle \xi \rangle_i - \langle \xi \rangle_{i-1}}{\xi_{i-1/2} - \langle \xi \rangle_{i-2}}, \quad c_{i-1,b} \equiv \frac{\langle \xi \rangle_{i-1} - \langle \xi \rangle_{i-2}}{\langle \xi \rangle_{i-1} - \xi_{i-3/2}} . \end{aligned} \quad (11)$$

Mirror expressions hold for right-side coefficients $c_{i,f}$, $c_{i,b}$. The slope limiter ϕ implements the modified van Leer formulation from [Mignone \(2014\)](#), ensuring monotonicity preservation through:

$$\phi(a, b, c, d) = \begin{cases} 0 & ab \leq 0 ; \\ \min \left[\frac{2|a|}{|a| + |b|}, \frac{2c}{c + d} \right] \operatorname{sgn}(a), & ab > 0 . \end{cases} \quad (12)$$

The nonlinear nature of slope limiters introduces fundamental challenges for chemical conservation: nonlinear reconstruction operators generally violate the proportionality required by eq. (2). This issue is resolved through stoichiometric space projection, reformulating the interface states as:

$$x_{i-1/2,l}^s = \langle x \rangle_{i-1}^s + \sum_r \mathcal{P}_r^s \chi_{i-1/2,l}^r , \quad (13)$$

with an analogous expression for $x_{i-1/2,r}^s$. The full interface reconstruction then follows:

$$x_{i-1/2}^s = x_{i-1/2,l}^s \Theta(\mathcal{F}_{i-1/2}^s) + x_{i-1/2,r}^s \Theta(-\mathcal{F}_{i-1/2}^s) . \quad (14)$$

This formulation exhibits features accuracy to arbitrary spatial order, as the correction terms χ are not limited to first order in eq. (9). Non-zero projections \mathcal{P}_χ introduce spatially varying corrections while preserving stoichiometric constraints, achieving formal second-order accuracy through the slope-limited derivatives. Note also that the cost of calculating \mathcal{P}_χ is at the order of $O(N^2)$, which is generally much quicker and free from numerical instabilities that are involved in the matrix inversion procedures.

2.2. Thermochemical Evolution

The thermochemical evolution in each computational cell is governed by a coupled system of stiff ordinary differential equations (ODEs) for chemical species densities $\{n^i\}$ and internal energy density ϵ :

$$\begin{aligned} \frac{dn^i}{dt} &= \sum_{j,k} \mathcal{A}_{jk}^i n^j n^k + \sum_j \mathcal{B}_j^i n^j , \\ \frac{d\epsilon}{dt} &= \Gamma(\{n^i\}, T) - \Lambda(\{n^i\}, T) , \end{aligned} \quad (15)$$

where \mathcal{A}_{jk}^i represents rate coefficients for binary reactions (formation or destruction of species i via interactions between j & k), \mathcal{B}_j^i captures unary processes affecting species i (especially photoionization, radioactive decay, etc.), and Γ and Λ denote volumetric heating and cooling rates, respectively. All reaction coefficients could be functions of the temperature T , which is thermodynamically coupled through $T = \epsilon/c_V(T, \{n^i\})$; c_V is the constant-volume heat capacity derived from the equation of state, as a function of the temperature itself and the abundances of all species $\{n^i\}$. The use of c_V (rather than c_P) reflects the operator-split approach where thermochemistry evolves independently from hydrodynamic work terms, as the hydrodynamic steps already resolve the contribution of volumetric work on its own.

Key numerical challenges typically arise from the stiffness, reflecting widely separated timescales between

chemical processes (e.g., fast ionizations versus slow molecular reactions). Non-linear dependence could also add to the difficulties, including the temperature dependence of rate coefficients $\mathcal{A}_{jk}^i(T)$, $\mathcal{B}_j^i(T)$ combined with thermal feedback through $\Gamma(T)$ and $\Lambda(T)$. In what follows, the numerical methodology is detailed for robust integration of this ODE system, emphasizing stability preservation and computational efficiency.

2.2.1. Reaction Rates and Jacobian Matrices

The integration of thermochemical ODEs necessitates careful evaluation of reaction rate coefficients, which are categorized roughly into three distinct types:

1. Two-body reactions with modified Arrhenius rate coefficients,

$$k(T) = k_0 \left(\frac{T}{T_0} \right)^\beta \exp \left(-\frac{T_0}{T} \right), \quad (16)$$

where (k_0, T_0, β) are parameters from astrochemical databases like [McElroy et al. \(2013\)](#). Associated heating/cooling rates follow similar temperature dependence.

2. Photoreactions governed by effective radiation flux $F_{\text{ph,eff}}$,

$$\zeta = \sum_i n^i \sigma_{\text{abs}}^i F_{\text{ph,eff}}(\lambda_{\text{abs}}^{-1}), \quad (17)$$

where $\lambda_{\text{abs}}^{-1} = \sum_i n^i \sigma_{\text{abs}}^i$ is the inverse absorption length. The flux $F_{\text{ph,eff}}$ self-consistently adapts to evolving chemical abundances (see also §3.2).

3. Tabulated reactions with numerically interpolated rates, where precomputed tables are read in to account for complex temperature dependence and local conditions (e.g., photon escape probabilities). At the beginning of the thermochemical computation, multi-dimensional tables are reduced to one-dimensional in T per cell, assuming fixed total mass density and elemental abundances during thermochemical steps.

For efficient solution of stiff ODEs using semi-implicit methods, the elements of Jacobian matrices,

$$\mathbf{J} \equiv \begin{bmatrix} \partial \dot{n}^i / \partial n^j, & \partial \dot{n}^i / \partial \epsilon \\ \partial \dot{\epsilon} / \partial n^j, & \partial \dot{\epsilon} / \partial \epsilon \end{bmatrix}, \quad (18)$$

are estimated analytically through (1) mass action derivatives:

$$\frac{\partial (\mathcal{A}_{jk}^i n^j n^k)}{\partial n^m} = \begin{cases} 2\mathcal{A}_{mm}^i n^m & (m = j = k) \\ \mathcal{A}_{jk}^i n^k & (m = j \neq k) \\ \mathcal{A}_{jk}^i n^j & (m = k \neq j) \end{cases}, \quad (19)$$

(2) thermal coupling terms (with analytical $\partial k / \partial T$ for Arrhenius and tabulated rates; the heat capacity derivative $\partial c_V / \partial n^i$ is typically neglected in the approximations for \mathbf{J}),

$$\frac{\partial k}{\partial \epsilon} = \frac{\partial k}{\partial T} \frac{\partial T}{\partial \epsilon} = \frac{1}{c_V} \frac{\partial k}{\partial T}, \quad (20)$$

and (3) radiation flux derivatives:

$$\frac{\partial F_{\text{ph,eff}}}{\partial n^i} \approx \sigma_{\text{abs}}^i \left(\frac{\partial F_{\text{ph,eff}}}{\partial \lambda_{\text{abs}}^{-1}} \right) \min \left\{ 1, \frac{n^i \sigma_{\text{abs}}^i}{\lambda_{\text{abs}}^{-1}} \right\}, \quad (21)$$

where the cutoff factor ensures dominant absorbers drive the derivative calculation. This hybrid analytical-numerical approach maintains $\mathcal{O}(N_{\text{reac}})$ complexity with respect to reaction number N_{reac} , while capturing essential Jacobian features for stable integration.

2.2.2. Pre-processing for Thermochemical Computations

The ODEs are solved as initial value problem, with the initial values taken from the step of fluid mechanical evolution that has just been finished. Note that Kratos uses total energy density for its Godunov solver; the thermal energy density ϵ is obtained by subtracting the kinetic energy density (plus magnetic energy density in magnetohydrodynamic simulations) from the total.

Post-advection chemical abundances $\{n^s\}$ require validation against numerical floors. If density floors apply, the abundances of species have to be rescaled. For temperature $T = \epsilon / c_V$, the check against effective temperature limits also applies to get rid of the potentially unphysical temperatures introduced by pressure floors in the hydrodynamic procedures. Prior to ODE integration, each cell undergoes:

- Rate table generation: Construct temperature-dependent rate interpolation tables, whose selection of temperature points should match the reaction scenarios.
- Dominant absorber identification: Determine species s^* maximizing photoabsorption contribution, which governs radiation flux derivative approximations during Jacobian construction

These preprocessing steps ensure thermodynamic consistency between advected and reacted states, and enhances numerical stability and computational efficiency through localized rate approximations.

2.2.3. Post-processing

Prior to updating the thermochemically evolved abundances and thermal energy density for subsequent fluid mechanical steps, several post-processing procedures

must be applied to each computational cell. These safeguards prevent unphysical outcomes from contaminating the entire simulation.

Frequent minor numerical artifacts require systematic correction, which mainly involved floating-point precision artifacts (particularly pronounced in GPU-accelerated computations using single-precision arithmetic), and occasional negative abundances due to numerical dispersions. The regularization pipeline implements three-stage correction:

1. If some species have negative abundances, their abundances are set to zero;
2. Abundances of elements are calculated for the initial and final states of thermochemical evolution. In the final state, the abundances in the single-element species are adjusted to compensate the differences. This step corrects the violation in element abundances brought by step 1;
3. If step 2 causes negative abundances in some single-element species, the most abundant compound species is disintegrated into elements just sufficiently to correct this. As the thermochemical reaction rates generally follow the mass-action law, this will cause minimal impacts on the behaviors of subsequent processes.

For cells where the ODE solver reports significant convergence failures in thermochemical calculations, or where results exhibit non-physical characteristics (e.g., NaN values, significant negative abundances, or substantial elemental conservation violations), a retry procedure is initiated using identical initial conditions but with reduced initial time step size and enhanced step size control parameters. Persistent failures trigger either reversion to pre-evolution values (as specified in initialization parameters), or a full simulation termination.

2.3. GPU-Optimized Algorithm

The computationally intensive nature of thermochemical ODE systems motivates implementation optimizations for modern heterogeneous architectures. While these ODE solutions remain expensive per-cell, their inherent embarrassingly parallel structure enables efficient acceleration. Each computational cell's thermochemical evolution is assigned to a dedicated thread block, leveraging the massive parallelism ability of heterogeneous devices. Because of the special heterogeneous architectures, the algorithms should be adjusted to optimize their performances, especially by utilizing the single-instruction multiple-threads (SIMT) schemes.

2.3.1. Reaction Rates and Jacobian Matrices

The evaluation of reaction rates and Jacobian matrices employs SIMT-optimized kernel design. Each thread computes one reaction's contribution to the overall reaction rate vector, and thread blocks process reactions in batches matching warp size (typically 32 or 64 reactions per batch),

$$\text{Batch Size} = \min \{S_{\text{warp}}, N_{\text{reac}} - kS_{\text{warp}}\} , \quad (22)$$

where S_{warp} is the warp size, and k represents completed batches. Excess threads remain inactive during final partial batches to avoid inconsistent calculations. Shared memory buffers are applied to eliminate the high-latency global memory access during rate accumulations. Results are accumulated by each thread via atomic operations (using the atomicAdd interface) to prevent race conditions.

2.3.2. Solving Linear Systems: LU Decomposition with SIMT

The computational bottleneck in semi-implicit ODE solvers emerges from solving numerous small-scale linear systems, typically involving 10 – 30 chemical species per cell, across massive ensembles of computational cells. Conventional GPU-optimized linear algebra routines prove suboptimal for this specific workload pattern, as they primarily target individual large matrices, dense or sparse, rather than concurrent batches of small systems. This architectural mismatch necessitates custom implementation strategies tailored to the single-instruction multiple-threads (SIMT) paradigm.

The implementation in Kratos employs Crout's algorithm with row pivoting for LU decomposition (Press et al. 2002), specifically adapted for GPU architectures. As detailed in Algorithm 1, the computation follows a thread-parallel approach where all threads execute identical instructions while maintaining individual thread indices i . Each thread operates on shared matrix a_{ij} and vector v_i data structures, with explicit synchronization barriers enforced at critical computation stages (lines 5, 8, and 11) to resolve data dependencies within matrix groups. Following successful LU decomposition with permutation tracking, the subsequent backward substitution phases implement standard parallel reduction patterns across thread blocks. The SIMT architecture proves particularly effective for this workload, as the uniform instruction flow across threads minimizes warp divergence while maximizing memory coalescing during matrix element access.

3. RAY TRACING MODULE

Algorithm 1: Parallel LU decomposition of matrices on multi-thread devices

Data : Matrix to be decomposed a_{ij} (size $N \times N$)
Result: LU-decomposed matrix stored in a_{ij} ;
 Permutation vector p_i .

- 1 $i \leftarrow$ thread index ($0 \leq i \leq N - 1$) ;
- 2 $v_i \leftarrow$ maximum absolute value in the i th row of a_{ij}
- 3 **for** $j \leftarrow 0$ to $N - 1$ **do**
- /* Compute U and unrescaled L */
- for** $k \leftarrow 0$ to $\min\{i - 1, j - 1\}$ **do**
- $a_{ij} \leftarrow a_{ij} - a_{ik}a_{kj}$;
- /* Pivoting: Let diagonals hold greatest possible absolute value */
- synchronize threads;
- if** $i \geq j$ **then** $t_i \leftarrow |a_{ij}|/v_i$;
- $i_{\max} \leftarrow$ index for the maximum t_i with $i \geq j$;
- synchronize threads;
- if** $j \neq i_{\max}$ **then** swap($a_{i_{\max}, i}, a_{ji}$);
- if** i is 0 **then** swap($v_{i_{\max}}, v_j$), $p_i \leftarrow i_{\max}$;
- /* Rescale L */
- synchronize threads;
- if** $j < i$ **then** $a_{ij} \leftarrow a_{ij}/a_{jj}$;
- 13 **end**

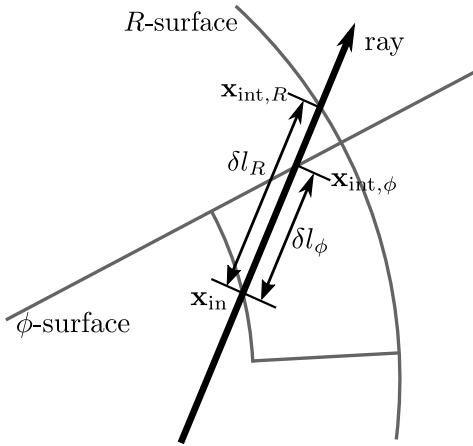


Figure 1. Example of comparing δl_ϕ and δl_R in cylindrical mesh, for the ray passing through a cell. This is a top-down view with z -related quantities omitted for clarity. Grey lines and curves indicate the excerpts of coordinate surfaces and boundaries of the cell concerned.

Radiation fundamentally governs the thermal and chemical states of astrophysical fluids in many cases, serving as critical input to thermochemical calculations. The ray tracing module in Kratos applies direct ray-tracing calculations for radiation fields in which scattering is of secondary importance. Although the extension to a full Monte-Carlo radiation scheme seems straightforward, the implementation have been discussed by Yang & Wang (2025) in details.

3.1. Ray tracing on Structured Meshes

The determination of photon propagation paths is the central geometric component in ray-tracing calculations. For consistent three-dimensional ray tracing, precise identification of a ray's entry and exit points across computational cells is essential. Each cell interface is mathematically described by six surfaces $\{S_i(\mathbf{x}) = 0\}$ where $i = 1, \dots, 6$, with \mathbf{x} denoting spatial coordinates. Given an initial penetration point \mathbf{x}_0 and propagation direction \hat{r} (where $|\hat{r}| = 1$), the ray trajectory follows the parametric form $\mathbf{x}(t) = \mathbf{x}_0 + \hat{r}\delta l$ for $\delta l \geq 0$. The set of six equations,

$$S_i(\mathbf{x}_0 + \delta l_i \hat{r}) = 0 ; \quad i = 1, \dots, 6 , \quad (23)$$

are solved for $\{\delta l_i\}$. In Cartesian coordinates:

$$0 = x_{d,i}\delta l_i + (x_{\text{in},i} - x_{\text{int},i}) \quad (i = 1, 2, 3 \text{ for } x, y, z) , \quad (24)$$

where variables with subscript “in” stands for the point at which the ray gets into the cell, the subscript “ d ” indicates the *Cartesian* components of the direction vector \hat{r} , and the subscript “int” denotes the coordinate value of the surface to intercept the current ray. In cylindrical coordinates:

$$\begin{aligned} 0 &= (x_d^2 + y_d^2)\delta l_R^2 + 2(x_{\text{in}}x_d + y_{\text{in}}y_d)\delta l_R + (R_{\text{in}}^2 - R_{\text{int}}^2) ; \\ 0 &= (x_d \tan \phi_{\text{int}} - y_d)\delta l_\phi + (x_{\text{in}} \tan \phi_{\text{int}} - y_{\text{in}}) ; \\ 0 &= z_d\delta l_z + (z_{\text{in}} - z_{\text{int}}) . \end{aligned} \quad (25)$$

In spherical polar coordinates:

$$\begin{aligned} 0 &= \delta l_r^2 + 2\mathbf{x}_{\text{in}} \cdot \hat{\mathbf{r}}\delta l_r + (r_{\text{in}}^2 - r_{\text{int}}^2) . \\ 0 &= (\cos^2 \theta_{\text{int}} - z_d^2)\delta l_\theta^2 + 2(\cos^2 \theta_{\text{int}}\mathbf{x}_{\text{in}} \cdot \hat{\mathbf{r}} - z_i z_d)\delta l_\theta \\ &\quad + (\cos^2 \theta_{\text{int}} - \cos^2 \theta_{\text{in}})r_{\text{in}}^2 ; \\ 0 &= (x_d \tan \phi_{\text{int}} - y_d)\delta l_\phi + (x_{\text{in}} \tan \phi_{\text{int}} - y_{\text{in}}) . \end{aligned} \quad (26)$$

When solving these geometric equations for ray propagation, the absence of real positive solutions to δl indicates non-intersection with the corresponding coordinate surface, allowing such cases to be safely disregarded. For problems with reduced dimensionality or cells containing degenerate surfaces (e.g., polar wedges in spherical grids), the system (23) solves fewer equations while maintaining three-dimensional representations of position vector \mathbf{x}_0 and direction vector \hat{r} . It is worth noting that multiple roots may emerge in curvilinear coordinate systems due to quadratic surface expressions (eqs. 25, 26), requiring explicit consideration. The exit point from each cell is determined by identifying the minimal positive solution δl_{\min} among $\{\delta l_j\}$

corresponding to surface index j . Negative solutions indicate unphysical backward propagations, which have to be discarded. Note also that $\delta l = 0$ roots can naturally emerge when there are more than one intersection with cell surfaces, while these solutions indicating the point at which the ray arrives into the current cell should also be excluded from the ray propagation solution. The updated propagation origin becomes $\mathbf{x}_0 + \delta l_{\min} \hat{r}$, initiating iterative traversal until domain exit. An example of this ray-tracing approach on spherical polar grids is illustrated in Figure 2, in which the direction of incoming rays are still parallel to the $x - y$ plane but tilted to $\theta = \arctan(0.1)$ with the horizontal axis. Such tilt exhibits the correct propagation results, where multiple intersections between rays and their current single cell surfaces are involved.

Photons within each ray are characterized by energy-dependent counts $N_{\text{ph,init}}(h\nu)$, assigned per directional emitter. For instance, from an isotropic point sources, the initialization follows,

$$N_{\text{ph,init}}(h\nu) = L_*(h\nu) \frac{\Delta\Omega}{4\pi} \delta t, \quad (27)$$

where $L_*(h\nu)$ denotes spectral luminosity of the source, $\Delta\Omega$ the ray's solid angle, and δt the timestep duration. Photon absorption within cells incorporates mean free path $\lambda_{\text{abs}}(h\nu)$ and effective flux calculation via path-averaged integration:

$$\begin{aligned} F_{\text{ph,eff}}(h\nu) &\simeq N_{\text{ph,in}}(h\nu) \left(\frac{\delta l_{\min}}{\delta V \delta t} \right) \left(\int_{\text{in}}^{\text{out}} ds \right)^{-1} \\ &\quad \times \int_{\text{in}}^{\text{out}} ds \exp[-\delta l_{\min}/\lambda_{\text{abs}}(h\nu)] \\ &= N_{\text{ph,in}} \left(\frac{\delta l_{\min}}{\delta V \delta t} \right) \left\{ \frac{1 - \exp[-\delta l_{\min}/\lambda_{\text{abs}}]}{\delta l_{\min}/\lambda_{\text{abs}}} \right\}. \end{aligned} \quad (28)$$

Here δV represents cell volume, with flux asymptotically approaching $N_{\text{ph,in}} \delta l_{\min}/(\delta V \delta t)$ in optically thin regimes ($\delta l_{\min}/\lambda_{\text{abs}} \rightarrow 0$) and scaling inversely with optical depth at high absorption. Multi-ray contributions sum across energy bins using (28). Photon depletion follows exponential attenuation:

$$N_{\text{ph,out}}(h\nu) = N_{\text{ph,in}}(h\nu) \exp[-\delta l_{\min}/\lambda_{\text{abs}}(h\nu)], \quad (29)$$

while accumulated column densities along propagation paths provide critical inputs for subsequent thermochemical rate calculations. It is noted that, although the discussions are introduced assuming an isotropic source, application of the ray tracing system is not limited to this simplest case. While Figure 2 presents an example

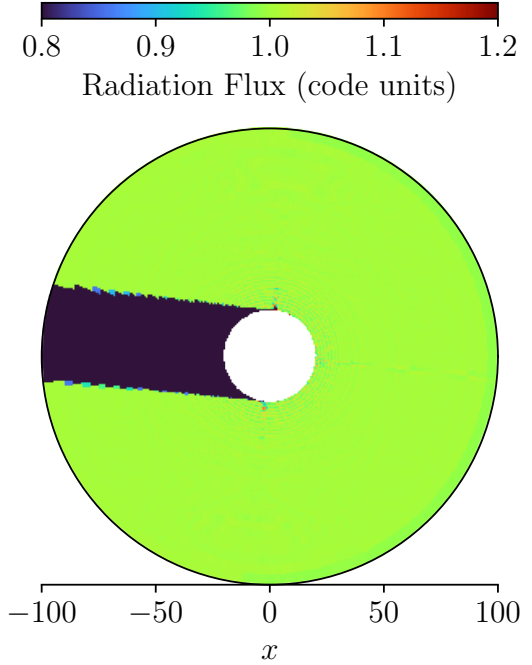


Figure 2. Test example of ray tracing on a spherical polar grid, with the radiation flux (at unitary intensity in code units) incidented at a $\theta = \arctan(0.1)$ angle with the horizontal axis (§3.1). The shadow behind the central blank zone can be clearly observed.

of parallel lights, Yang & Wang (2025) have also verified the same module for ray tracing on the cases for extended sources (equivalent to $\sim 10^6$ sources distributed across the simulation domain).

3.2. Radiation-matter Interactions

In the Kratos computational framework, it is assumed spatially uniform species concentrations within individual cells by default. For monochromatic radiation traversing a cell with photon luminosity L , the photon deposition rate derives from Beer-Lambert attenuation as $L[1 - \exp(-\sigma n \delta l)]$, where σ denotes reaction cross-section, n reactant concentration, and δl optical path length. Normalization by reactant count $n \delta V$ (with δV as cell volume) yields the reaction rate coefficient:

$$k \simeq \frac{L[1 - \exp(-\sigma n \delta l)]}{n \delta V} = \left(\frac{L \sigma \delta l}{\delta V} \right) \left(\frac{1 - \exp(-\tau)}{\tau} \right), \quad (30)$$

where $\tau \equiv \sigma n \delta l$ represents the local optical depth of absorption. This reduces to $k = L \sigma \delta l / \delta V$ in optically thin regimes ($\tau \rightarrow 0$). Generalization to multi-reaction, multi-ray systems employs the formalism with multiple indices for reactant species i , radiation rays j , and pho-

ton energy bins k ,

$$k_i = \sum_{j,k} k_{ijk}^{(0)} \left[\frac{1 - \exp(-\hat{\tau}_{jk})}{\hat{\tau}_{jk}} \right], \quad (31)$$

$$k_{ijk}^{(0)} \equiv \frac{L_{jk} \sigma_{ik} \delta l_j}{\delta V}, \quad \hat{\tau}_{jk} \equiv \sum_i n_i \sigma_{ik} \delta l_j,$$

where L_{jk} specifies photon flux per ray-energy pair, σ_{ik} energy-dependent cross-sections, and δl_j ray-specific path lengths. These rates directly populate the matrix $\{B_j^i\}$ in (15), with reactant depletion ($-k_i$) and product generation ($+k_i$) terms.

Temporal integration over timestep δt quantifies species concentration changes and energy-resolved photon absorption:

$$\delta L_{jk} = \sum_i \left(\frac{\sigma_{ik} \delta l_j}{\mathcal{N}_i} \int_t^{t+\delta t} k_i n_i \, dt \right), \quad (32)$$

$$\mathcal{N}_i \equiv \sum_{j,k} \sigma_{ik} \delta l_j,$$

where \mathcal{N}_i normalizes cross-section-weighted path lengths. The attenuated photon fluxes $L_{jk} \leftarrow L_{jk} - \delta L_{jk}$ propagate iteratively through downstream cells, coupling rays for photons to chemical evolution via cumulative optical depth updates.

4. CODE VERIFICATIONS

This section provides code verifications for the ray-tracing and thermochemistry modules combined. It is noted that the parallelization approach of the Kratos framework is built upon the heterogeneous architecture detailed in Wang (2025a), while the specific implementation and performance scaling of the ray-tracing radiation module are documented in details in Yang & Wang (2025). Within the context of the simulations presented in this work, which emphasize real-time non-equilibrium thermochemistry, the computational overhead of radiation transport is secondary to that of the stiff chemical ODE integration. Consequently, the comprehensive scaling tests and performance metrics provided in this manuscript primarily reflect the efficiency and throughput of the thermochemical solver, as it represents the dominant computational bottleneck in these coupled astrophysical applications.

4.1. Advection Tests

To evaluate the conservation properties of the advection algorithms described in §2.1, and specifically to demonstrate the necessity of implementing conservative higher-order reconstruction for chemical species (rather than donor-cell methods) in Kratos, a one-dimensional

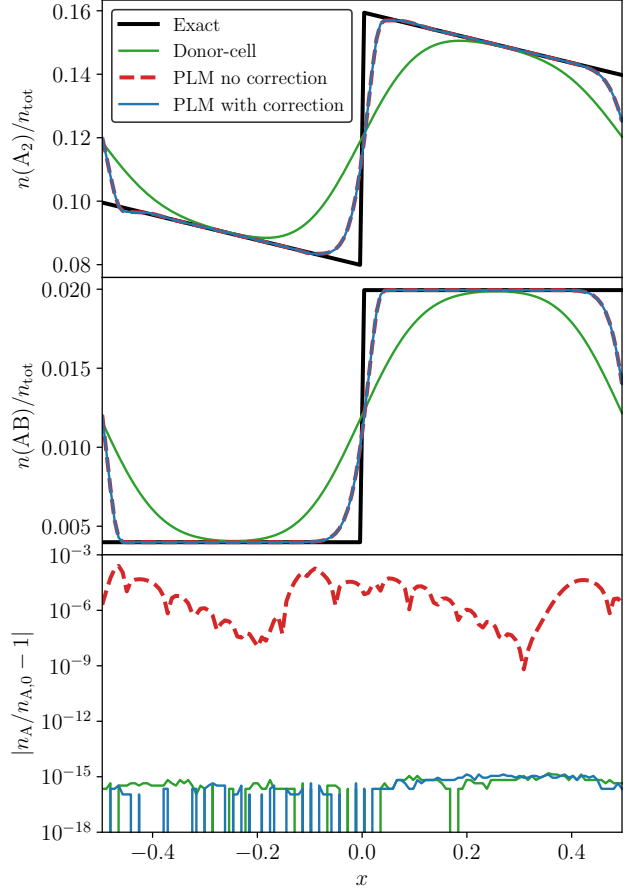


Figure 3. Test results of different advection schemes (see §4.1). The advection results (in number density ratios relative to n_{tot}) using different algorithms are presented in the upper two panels at $t = 1$ for two representative species, compared to the exact solution in heavy solid lines. Note that the lines for PLM with and without stoichiometric corrections overlap each other. The bottom panel shows the violation of elemental abundance conservation in comparison to the exact solutions.

test case is implemented within the spatial domain $x \in [-0.5, 0.5]$, discretized into 128 uniform zones with periodic boundary conditions. The fluid maintains constant mass density ($\rho = 1$) and pressure ($p = 1$) in code units, while advecting left-to-right at velocity $v = 1$. Four passive chemical species (A, A₂, AB, B) track two conserved elements (A and B), with initial abundance profiles defined as:

$$n_A = 0.49\Theta(-x) + 0.05\Theta(x) + 0.2x, \quad (33)$$

$$n_{A_2} = 0.20\Theta(-x) + 0.40\Theta(x) - 0.1x,$$

$$n_{AB} = 0.01\Theta(-x) + 0.05\Theta(x),$$

$$n_B = 0.09\Theta(-x) + 0.05\Theta(x),$$

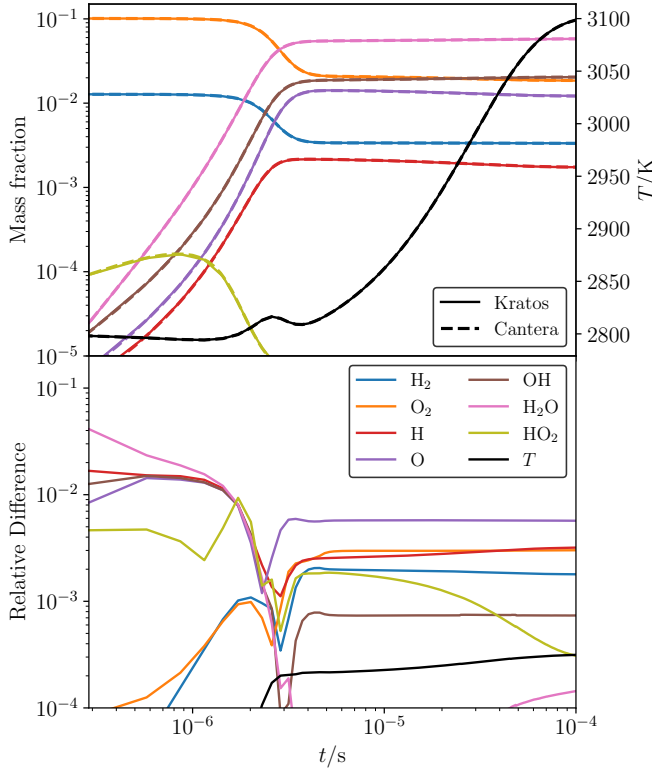


Figure 4. Thermochemical reaction tests for the burning of molecular hydrogen with oxygen (§4.2), comparing the Kratos mixed-precision results (solid lines) with the Cantera ones (dashed lines). The upper panel exhibits the evolution of different variables (distinguished by line colors), including the mass fraction of chemical species (the left ordinate, in logarithm scale) and the temperature (the right ordinate, in linear scale), while the lower panel shows the relative differences of the mass fractions and the gas temperature.

where $\Theta(x)$ denotes the Heaviside step function. The system evolves for $t = 1$, which should theoretically recover initial conditions due to periodicity.

Figure 3 reveals two key observations. First, the piecewise linear method (PLM) reconstruction scheme significantly reduces numerical diffusion compared to donor-cell approaches, regardless of conservation corrections. Second, uncorrected PLM introduces substantial element A conservation errors ($\sim 10^{-3}$ per ~ 300 step), which would grow to $\sim 10^{-1}$ after $\sim 10^5$ timesteps, being even more catastrophic for longer-term thermochemical simulations. In contrast, both donor-cell and corrected PLM schemes maintain species conservation within machine precision ($\lesssim 10^{-15}$ relative error), demonstrating the necessity of the flux correction mechanism described in §2.1.

4.2. Single-point Thermochemistry Tests

To validate the thermochemical solver in the absence of hydrodynamic effects, single-point ignition tests were conducted for a stoichiometric mixture of molecular hydrogen (H_2) and molecular oxygen (O_2) diluted in argon (Ar). The simulations employed the GRI-Mech 3.0 chemical kinetic mechanism (Smith et al. 2025), using the submechanism subtracted by Cantera (Goodwin et al. 2022) prioritizing high-temperature combustion processes. The submechanism is a combustion-focused network comprising 12 species (including radicals and intermediates such as H, O, OH, and HO_2) and 116 elementary reactions (including inverse reactions). The initial conditions were defined as a molar composition of 20% H_2 , 10% O_2 , and 70% Ar, preheated to $T = 2800$ K to accelerate ignition. The evolution track is simulated using both the Kratos framework and the benchmark tool Cantera, with a focus on tracking species concentrations and temperature until thermochemical equilibrium was achieved.

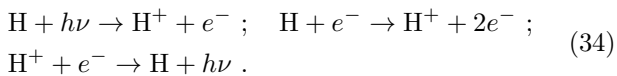
A key consideration in high-temperature combustion simulations is the accurate representation of heat capacity (c_V) variations. At temperatures exceeding $\sim 10^3$ K, vibrational modes in polyatomic molecules (e.g., H_2O , O_2) become thermally activated, leading to a nonlinear rise in c_V with increasing temperature. The Kratos solver therefore includes an option to incorporate this physics through NASA polynomial formulations (Muñoz et al. 2010) using updated parameters adopted by Cantera (Goodwin et al. 2022), which express c_V into piecewise sixth-order polynomial functions across discrete temperature intervals (typically 300 – 1000 K and 1000 – 3500 K). These polynomials are derived from spectroscopic data and statistical thermodynamics, enabling precise calculations of enthalpy and entropy. To quantify the impact of this model, a control simulation assuming constant heat capacity (frozen at the 300 K values) was performed, resulting in a $\sim 15\%$ overprediction of equilibrium temperature due to the underestimation of heat capacities. This error arises from neglecting the energy partitioned into vibrational modes, which effectively increases the system's thermal inertia. The integration of NASA polynomials into equation-of-state class template of Kratos ensures that such temperature-dependent effects are rigorously captured, a necessity for predictive combustion modeling.

Figure 4 demonstrates high consistency between the Kratos and Cantera results across the combustion timeline. During the ignition phase ($t \lesssim 10^{-6}$ s), minor discrepancies in trace species (e.g., H, O, OH) with mass fractions below 10^{-3} were observed, exhibiting relative differences on the order of $\sim 10^{-2}$. These deviations are attributed to numerical sensitivities in resolv-

ing fast radical-driven reactions during the induction period. However, as the system approached equilibrium, the mass fractions of major species—H₂O (primary product), unburned H₂, and residual O₂—converged to near-identical values in both solvers, with discrepancies limited to $\lesssim 10^{-3}$. Notably, the final equilibrium temperature computed by Kratos differed from Cantera by only 10^{-4} relative error, emphasizing the precision of the thermodynamic and ray-tracing models implemented in Kratos even using mixed-precision methods. The close agreement between Kratos and Cantera validates the former’s implementation of chemical kinetics, thermodynamic properties, and solver algorithms. The convergence of major species and temperature to near-machine precision at equilibrium also exhibits the robustness of Kratos semi-implicit solver and its adaptive substep control scheme.

4.3. Strömgren Sphere Tests

Strömgren sphere tests serve as a standard for validating numerical simulations of thermochemical reactions and radiation calculations in astrophysical scenarios. Such tests model the ionized regions around luminous sources of ionizing photons embedded in a neutral medium, providing a well-understood benchmark for comparing numerical methods against semi-analytic solutions. This work employs the Strömgren sphere test to evaluate the accuracy of the radiation-hydrodynamics framework, focusing on the interplay between photoionization, collisional processes, and radiative recombination in a simplified hydrogen-only chemistry network that only consist of atomic hydrogen (H), hydrogen ions (H⁺), and free electrons (e⁻).



At equilibrium, the thermal pressure inside the Strömgren sphere equals the ambient pressure of the surrounding neutral medium, given by the ambient hydrogen atom number density n_{amb} and temperature T_{amb} . The internal profiles of Strömgren spheres are also constrained by ionization, recombination, and thermodynamical conditions,

$$\begin{aligned} F &= \frac{\Phi}{4\pi r^2} e^{-\tau} , \quad \frac{d\tau}{dr} = n_{\text{H}}\sigma , \\ 0 &= n_{\text{H}}(1+x_e)k_{\text{B}}T - n_{\text{amb}}k_{\text{B}}T_{\text{amb}} , \\ 0 &= \alpha n_{\text{H}}^2 x_e^2 - k_{\text{ci}} n_{\text{H}}^2 x_e (1-x_e) - F\sigma n_{\text{H}}(1-x_e) , \quad (35) \\ 0 &= \lambda_{\text{rec}}\alpha n_{\text{H}}^2 x_e^2 + I_{\text{H}} k_{\text{ci}} n_{\text{H}}^2 x_e (1-x_e) \\ &\quad - (h\nu - I_{\text{H}})F\sigma n_{\text{H}}(1-x_e) . \end{aligned}$$

Here, F is the ionizing photon flux, Φ is the luminosity of ionizing photons, τ is the absorption optical depth, σ is

the photoionization cross-section, n_{H} is the total number density of hydrogen nuclei (including H and H⁺), $h\nu$ is the photon energy (assuming monochromatic radiation), and $I_{\text{H}} = 13.6$ eV is the ionization energy of hydrogen. The thermochemistry parameters are functions of temperature, including k_{ci} as the collisional ionization rate coefficient, α as the case-B recombination coefficient, and λ_{rec} as the cooling energy per recombination reaction,

$$\begin{aligned} k_{\text{ci}} &= 1.05 \times 10^{-9} \text{ cm}^3 \text{ s}^{-1} \left(\frac{T}{300 \text{ K}} \right)^{1/2} e^{-I_{\text{H}}/k_{\text{B}}T} , \\ \alpha &= 3.5 \times 10^{-12} \text{ cm}^3 \text{ s}^{-1} \left(\frac{T}{300 \text{ K}} \right)^{-0.75} , \\ \lambda_{\text{rec}} &= \left[0.684 - 0.0416 \ln \left(\frac{T}{10^4 \text{ K}} \right) \right] k_{\text{B}}T . \end{aligned} \quad (36)$$

adopting the data and expressions in [McElroy et al. \(2013\)](#) and [Draine \(2011\)](#). Eqs. (35) with (36) can be solved semi-analytically to obtain the hydrodynamics, radiation, and thermochemical profiles, by integrating from the center ($r = 0$) to the location that the absorption optical depth reaches $\tau = 10^2$ (other terminal τ values are tested to verify that the results are not affected).

Using the radiation and thermochemical module described in §2 and §3, a fiducial Strömgren sphere with parameters $\Phi = 10^{49} \text{ s}^{-1}$, $T_{\text{amb}} = 10^4 \text{ K}$, and $n_{\text{amb}} = 130 \text{ cm}^{-3}$ is solved by a Kratos. The simulation locates the radiation source at the origin point of a mesh with 64^3 zones, covering the $[0, 16 \text{ pc}]^3$ spatial region (thus $\Delta x = 1/4 \text{ pc}$), and is evolved through the steady state with constant pressure at boundaries given by n_{amb} and T_{amb} . Note that a relatively low resolution is adopted intentionally to demonstrate the accuracy and robustness of the system under limited resolution. Figure 5 exhibits excellent agreement between the numerical results and semi-analytic profiles within the ionized region, with relative deviations typically below $\sim 5\%$. Discrepancies emerge in the innermost cells ($r < 1 \text{ pc}$), where the radiation flux is underestimated by up to $\sim 50\%$. This deviation is confirmed to be arising from the Cartesian grid’s limited ability to resolve spherical symmetry at low radii, where the misalignment of the grid with the intrinsic geometry becomes significant. Despite this, the outer regions, where ionization and thermal structures are most dynamically relevant, show robust convergence, validating the numerical treatment of ionization and radiation co-evolved with hydrodynamics.

Figure 6 presents the simulated Strömgren radii R_s , which agree with semi-analytic predictions to within

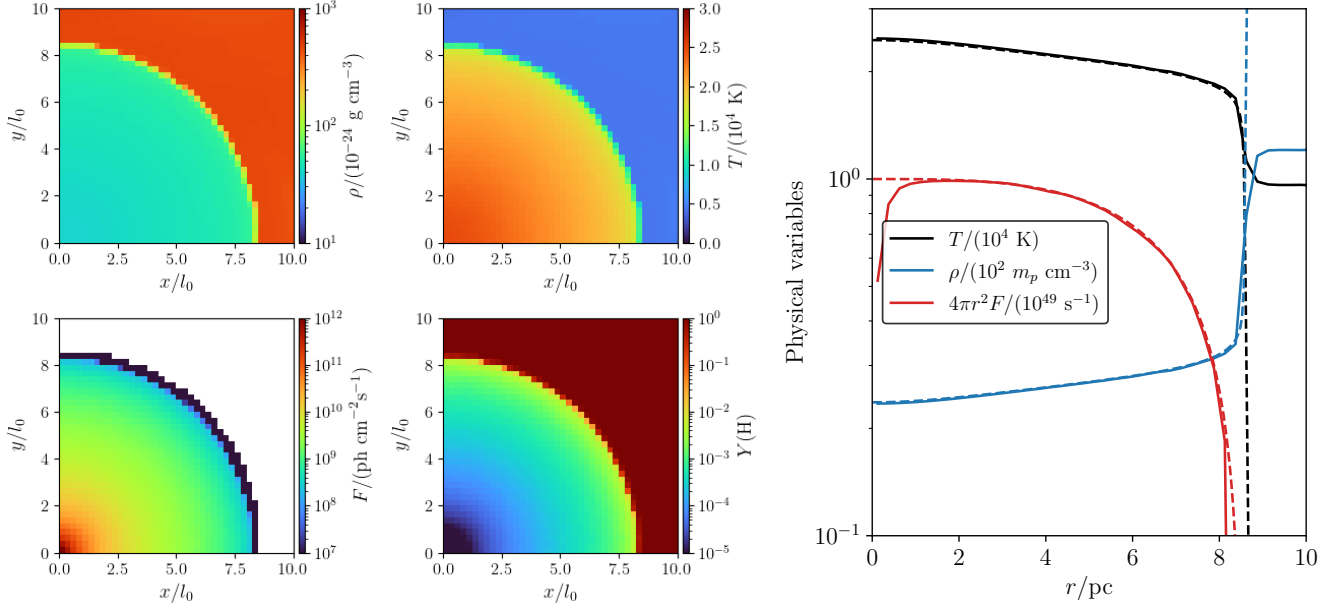


Figure 5. Hydrostatic profiles of the Strömgren sphere test using the fiducial set of parameters (see §4.3). The left four colormap panels, marked with the code unit length $l_0 = \text{pc}$, show the slices at $z = 0$ for mass density ρ , temperature T , ionizing photon flux F , and the mass fraction of neutral hydrogen $Y(\text{H})$. The right panel illustrates the profiles along the radial line along the z -axis, comparing the results by Kratos (solid lines) with the semi-analytic solutions (dashed lines).

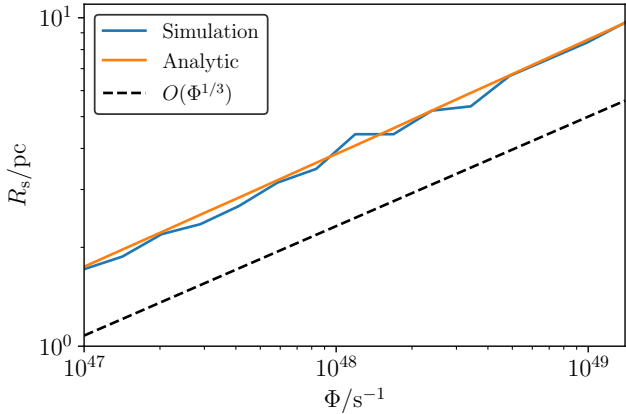


Figure 6. Radii of Strömgren spheres (R_s) under different ionizing photo luminosities (Φ), comparing the simulation results to the analytic solutions. The $R_s \propto \Phi^{1/3}$ power-law is shown in a heavy dashed line for reference.

$\sim 5\%$ across two orders of magnitude in ionizing photon luminosity Φ (from 10^{47} s^{-1} through 10^{49} s^{-1}). This consistency also verifies the ability of Kratos framework to accurately capture the $R_s \propto \Phi^{1/3}$ scaling of the Strömgren radius, a fundamental relation in HII region physics. The minor deviations at low Φ also stem from the geometry, when the sphere radii are small and the discreteness of the mesh cells cause the step growth when Φ increases. The Strömgren sphere test confirms that the Kratos framework accurately reproduces key physical processes in ionized plasmas within the sphere, including

chemical reactions (ionization balance), thermodynamics, and radiation.

4.4. Detonation Tests

Detonation flows represent one of the most rigorous benchmarks for reacting flow simulation codes, as they involve complex interactions between hydrodynamics, chemical reactions with multiple chemical species, and thermodynamics associated with these reactions. A detailed validation is carried out for the Kratos simulation framework simulating steady-state detonations, comparing numerical results against semi-analytic solutions computed with the Shock and Detonation Toolbox (SDT hereafter; Muñoz et al. 2010) constructed on the top of Cantera. These tests not only assess the accuracy of the thermochemical network but also evaluate the code ability to resolve shock propagation, and the chemistry at and in the downstream of detonation shocks in multi-dimensional configurations. Ideally, each set of upstream conditions corresponds to a unique set of downstream conditions, and can be described by semi-analytic solutions. To develop into this steady-state detonation described exactly by semi-analytic solutions, however, the shock wave has to propagate through a very long spatial range to converge to the steady state. Therefore, the simulation condition in these detonation tests are setup in the shock frame, while the upstream gas is fed into the system from the boundary on the right-hand side.

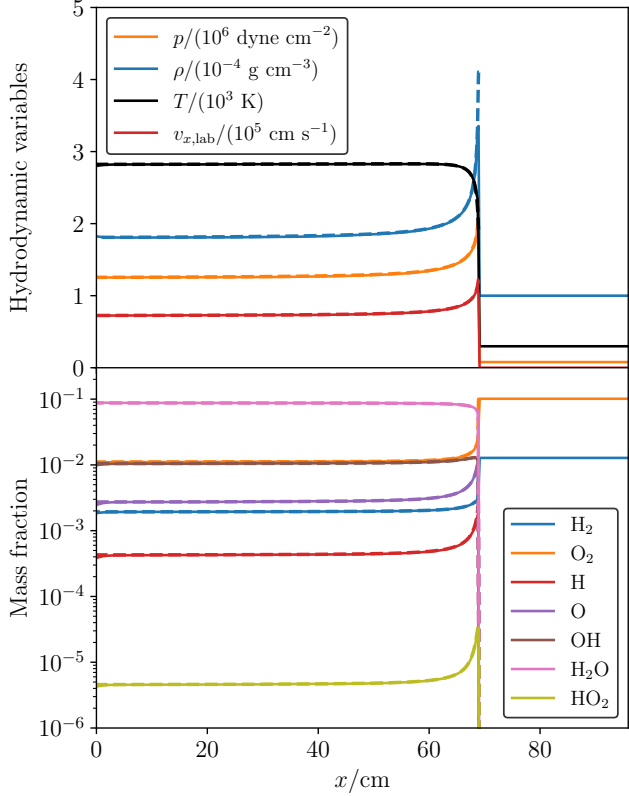


Figure 7. Hydrodynamic profiles (upper panel) and mass fractions of chemical species (lower panel) of the fiducial detonation test (see §4.4), comparing the Kratos simulation results (solid lines) with the semi-analytic results yielded by SDT (dashed lines). Note that the presented velocity is measured in the lab-frame.

4.4.1. Comparisons with the SDT Benchmark

The detonation tests are configured in one spatial dimension (with additional verification in higher dimensions) using the thermochemical network described in §4.2. The simulations are initialized in the shock frame, where upstream gas is fed into the system from the right-hand boundary, while the left-hand boundary adopts outflow conditions. This setup ensures that the shock wave propagates through a sufficiently long spatial distance to achieve steady-state conditions, which are critical for meaningful comparisons with semi-analytic solutions. For the fiducial simulation carried out on a $(x/\text{cm}) \in [0, 96]$ domain covered by 512 simulation zones along the x -axis, the upstream gas consists of 20% H_2 , 10% O_2 , and 70% Ar by molar fraction, with a temperature $T_0 = 298 \text{ K}$ and mass density $\rho_0 = 10^{-4} \text{ g cm}^{-3}$. At $t = 0$, the region with $x < 76.8 \text{ cm}$ is set uniformly to the post-shock values at $x \rightarrow -\infty$ for the density, temperature, and chemical abundances given by SDT, in order to trigger the shock, the chemical reactions,

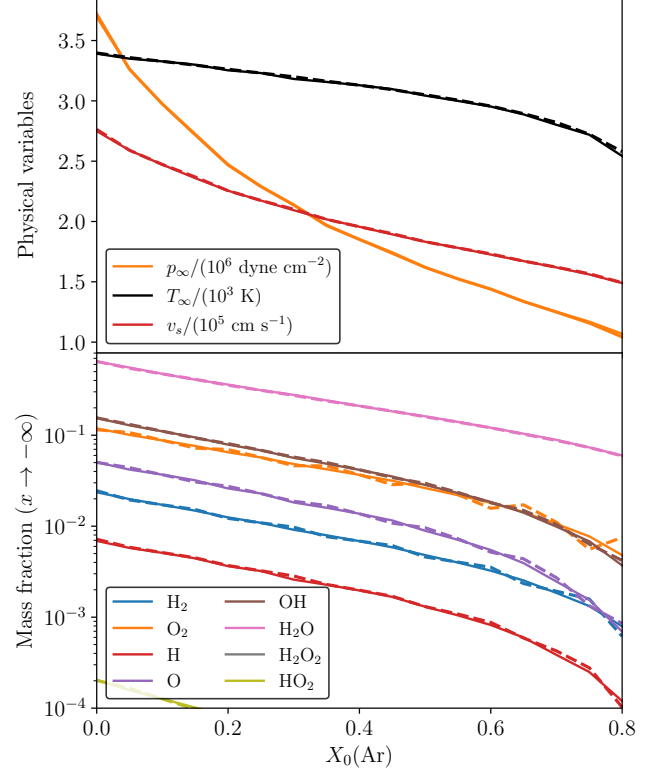


Figure 8. Hydrodynamic quantities (upper panel) and mass fractions of chemical species (lower panel) with different upstream molar fractions of argon $[X_0(\text{Ar})]$, showing the detonation shock speed v_s , and physical quantities at large distance in the detonation wave downstream (marked as $x \rightarrow -\infty$). The Kratos simulations (solid lines) are compared to the SDT results (dashed lines). Note that the mass fractions of low-abundance species at high $X_0(\text{Ar})$ are slightly unstable in the SDT outputs.

and to shape the detonation eventually. This approach ensures consistency between the numerical and semi-analytic frameworks, minimizing discrepancies arising from mismatched initial states.

Figure 8 shows the comparison between Kratos simulation results and SDT semi-analytic solutions, revealing excellent agreement across all hydrodynamic and thermochemical profiles. Relative errors in downstream variables (e.g., density, temperature, velocity) are consistently at the order of $\sim 0.1\%$, demonstrating the high fidelity of the numerical method. Most notably, the detonation speed—a critical parameter for validating shock propagation—deviates from the semi-analytic solution by no more than 0.3%. This precision underscores the framework's ability to resolve the intricate coupling between hydrodynamics and chemistry in detonation flows.

4.4.2. Accuracy under Various Conditions

To further validate the robustness of the framework, more tests are conducted to vary upstream Ar abundance systematically while maintaining stoichiometric ratios of H₂ and O₂. The downstream hydrodynamic variables (e.g., pressure, temperature) at sufficient distance from the detonation front (marked as $x \rightarrow -\infty$) agree with SDT results within $\sim 1\%$, confirming the predictive capability of Kratos across a range of upstream conditions. Minor discrepancies emerge in the mass fractions of chemical species with low abundance (e.g., OH, H₂O), which fluctuate by $\sim 10\%$ when computed using SDT. This behavior is attributed to the reliance of Cantera (as the backend of SDT) on operator-splitting methods, where thermodynamics and chemistry are solved in separate sub-steps. In comparison, Kratos employs a simultaneous solution approach (§2.2), which reduces numerical instabilities and produces smoother, more physically consistent results. This illustrates a key advantage of the Kratos framework in resolving complex reacting flows, particularly in regimes where minor species play significant roles.

4.4.3. Speed Tests in 3D

The detonation test series serves dual purposes—validating thermochemical accuracy and quantifying computational efficiency in Kratos. By extending the fiducial detonation setup to plane-parallel 3D geometry, the performance across various heterogeneous architectures is benchmarked and presented in Table 1. Contemporary GPUs demonstrate high computational throughput, with NVIDIA RTX 4090 achieving $\sim 1.7 \times 10^7$ cell s⁻¹ initial computation rates as shown in Table 1, along with a few other typical architectures. This outperforms CPU-based Cantera implementations by orders of magnitude ($\sim 10^6$ cell s⁻¹ with 8-core parallelization, and $\sim 10^5$ cell s⁻¹ on a single core). Comparisons with more CPU cores have also been conducted, yet the basic scaling remain the same. Note also that, on a typical contemporary multi-GPU server, one GPU usually corresponds to 8 or 16 CPU cores). It is also noted that, using identical codebases, the thermochemical module has been derived into thermonuclear reaction module, which have also been calibrated and tested for performance against artificial neural network methods in Zhang et al. (2025).

Compared to pure hydrodynamic simulations elaborated in Wang (2025a), thermochemical integration introduces $\sim 10^2$ slowdown due to stiff ODE solving with semi-implicit methods, as the sub-step controllers dynamically adjust temporal resolution, increasing iteration counts during chemically active phases. Despite this baseline cost, thermochemistry exhibits favorable

Table 1. Performance measurements based on the 3D detonation tests.

Programming Models and Devices	Computing Speed with Precision		
	Single	Mixed	Double
HIP-CPU*			
AMD Ryzen 5800X [†]			0.19
Qualcomm Snapdragon 888**			0.0089
NVIDIA CUDA			
RTX 3090	6.9	6.5	0.97
RTX 4090	21.6	17.1	2.4
RTX 4090 $\times 8^{\ddagger}$	114.9	112.4	16.3
Tesla A100	9.3	9.1	5.5
AMD HIP			
7900XTX	4.5	4.6	—***
MI100	1.52	1.56	—***

NOTE— Presenting the average over 10^2 steps. All tests cases are in 3D. Detailed setups see §4.4.

*: Only double precision results are concerned, as modern CPUs have almost the same single and double precision computing speeds.

†: Utilizing all 8 physical cores.

‡: Using 8 GPU cards on the same computing node, with the same simulation setup (i.e. showing the strong scaling).

**: Using termux (<https://termux.dev>) on Android operating system, utilizing one major physical core. Compile-time optimization are turned *off* because of the software restrictions of TBB on ARM CPUs.

***: Failed to launch on the AMD HIP model with full double precision, due to the lack of several double precision functions.

strong scaling characteristics. Mixed-precision implementations, together with the MPI-based inter-process data transfer schemes detailed in Wang (2025a), achieve $\sim 84\%$ parallel efficiency across 8 GPUs, contrasted with $\sim 50\%$ scaling for hydrodynamic-only calculations on equivalent hardware (see also Wang 2025a). This increase arises from thermochemistry’s embarrassingly parallel workload distribution, where most of the computing cycles remain local to individual cells. The remaining overhead still arises from global ray-tracing updates and MPI boundary exchanges.

5. DISCUSSIONS AND SUMMARY

The thermochemistry and ray tracing modules presented in this paper, based on the Kratos framework (Wang 2025b), provides a comprehensive and efficient solution for simulating complex reacting flows in astrophysical and other scenarios. By integrating consistent microphysics calculations with hydrodynamics, the Kratos framework overcomes limitations of previous approaches, such as computational inefficiencies and inconsistencies between thermochemistry and fluid dynamics.

Kratos allows full degrees of freedom to include thermochemical processes in the runtime by users. Key innovations incorporated in the thermochemistry and ray tracing modules of Kratos involve the heterogeneous-optimized algorithms of thermochemical evolution, ray-tracing, and chemical species advection, which enable high-performance simulations while ensuring element conservation and numerical stability. The stoichiometry-compatible scheme for the reconstruction of chemical species is applicable to higher order schemes of reconstruction that may involve non-linear functions, which removes the constraint of constant relative abundances of elements in other methods such as CMA, and accelerates the calculations by avoiding matrix inversions. The algorithms for solving thermochemical ODEs through parallel LU decomposition on SIMD devices also maximizes the efficiency to conduct reacting flow simulations on heterogeneous devices, especially GPUs.

The robustness and accuracy of Kratos are demonstrated through a series of rigorous tests, including chemical species advection, single-point thermochemical evolution, Strömgren sphere simulations, and detonation flow benchmarks. These tests validate the ability of Kratos to maintain elemental conservation, resolve complex hydrodynamic structures, and accurately model ionization fronts and combustion processes, with results closely matching benchmarks like against analytical results and semi-analytic benchmarks given by Cantera and SDT. In addition, the computing speed of Kratos with thermochemistry also outperforms CPU-based methods (used in e.g. Cantera), scaled at $\sim 10^2$ CPU cores using one contemporary GPU. The Kratos framework thus exhibits its versatility in addressing diverse astrophysical phenomena that involve thermochemistry with radiation as the underlying driving mechanisms.

Looking ahead, several directions for future work are envisioned to further enhance the capabilities of Kratos framework. The ray-tracing scheme described in §3 can be extended without too much efforts to solve the radiative transfer problems with scattering, which enables a much broader range of applications dealing with radiation-matter interactions. This module is also possible to be developed into a stand-alone distribution of Kratos that deals with scattering of polarized photons, which can be adopted by the exploration and interpretation of observations with polarization information (Yang

& Wang 2025). Machine learning techniques could be explored to accelerate thermochemical rate evaluations or optimize solver performance. For example, the DeepODE solver (Yao et al. 2025) is expected to further accelerates the reacting flow computations in Kratos. The current attempts of integrating DeepODE into Kratos shows that the machine learning solver performs better than the “traditional” solver (e.g. §2.2) when the stiffness of the thermochemical ODEs are high, while the traditional solver performs better than the machine learning methods in the low-stiffness secular evolution (Zhang et al. 2025). Extending support for nuclear reaction networks, complicated equations of state, and relativistic hydrodynamics would enable the studies of extreme physical and astrophysical phenomena, which has been already composed for the purpose of supernovae and compact object mergers, and will be described in separate papers (see also Zhang et al. 2025). In the “downstream” of the thermochemical modules, the integration with magnetic fields and non-ideal MHD effects would extend the applicability to magnetized jets and accretion disks, similar to the toolchain adopted in Wang et al. (2019); Yue et al. (2024). From the prospective of software engineering, improving user accessibility through Python interfaces will facilitate broader applications, and also allows for further interactions and integrations of other community-driven codes and modules.

Code availability: As Kratos is still being developed actively, the author will only provide the code upon requests and collaborations at this moment. While several important modules that are already mature have already been adopted and made public along with Wang et al. (2025), a more complete version of Kratos will be available publicly after further and deeper debugs are accomplished.

L. Wang acknowledges the support in computing resources provided by the Kavli Institute for Astronomy and Astrophysics in Peking University. The author thanks the colleagues for helpful discussions (alphabetical order): Xue-Ning Bai, Renyue Cen, Jeremy Goodman, Xiao Hu, Mordecai Mac-Low, Kengo Tomida, Haifeng Yang, Tianhan Zhang, and Yao Zhou, for helpful discussions and useful suggestions. Special thanks to Tianhan Zhang for the discussions on the physics of thermochemical detonation.

REFERENCES

Draine, B. T. 2011, Physics of the Interstellar and Intergalactic Medium (Princeton University Press)

Fang, M., Wang, L., Herczeg, G. J., et al. 2023, Nature Astronomy, 7, 905

Glover, S. C. O., Federrath, C., Mac Low, M.-M., & Klessen, R. S. 2010, MNRAS, 404, 2

Goodwin, D. G., Moffat, H. K., Schoegl, I., Speth, R. L., & Weber, B. W. 2022, Cantera: An Object-oriented Software Toolkit for Chemical Kinetics, Thermodynamics, and Transport Processes, v2.6.0, Zenodo, doi:10.5281/zenodo.6387882

Hu, X., Zhu, Z., Okuzumi, S., et al. 2019, ApJ, 885, 36

McElroy, D., Walsh, C., Markwick, A. J., et al. 2013, A&A, 550, A36

Mignone, A. 2014, Journal of Computational Physics, 270, 784

Muñoz, C., Butler, R., Narkawicz, A., Maddalon, J., & Hagen, G. 2010, A Criteria Standard for Conflict Resolution: A Vision for Guaranteeing the Safety of Self-Separation in NextGen, Technical Memorandum NASA/TM-2010-216862, NASA, Langley Research Center, Hampton VA 23681-2199, USA

Nemer, A., Goodman, J., & Wang, L. 2020, ApJ, 904, L27

Plewa, T., & Müller, E. 1999, A&A, 342, 179

Press, W. H., Teukolsky, S. A., Vetterling, W. T., & Flannery, B. P. 2002, Numerical recipes in C++ : the art of scientific computing (Cambridge University Press, Cambridge)

Smith, G. P., Golden, D. M., Michael, F., et al. 2025, GRI-Mech, http://www.me.berkeley.edu/gri_mech/, ,

Stone, J. M., Tomida, K., White, C. J., & Felker, K. G. 2020, ApJS, 249, 4. <https://iopscience.iop.org/article/10.3847/1538-4365/ab929b>

Wang, L. 2025a, arXiv e-prints, arXiv:2501.02317

—. 2025b, ApJS, 277, 63

Wang, L., Bai, X.-N., & Goodman, J. 2019, ApJ, 874, 90

Wang, L., & Dai, F. 2018, ApJ, 860, 175

—. 2019, ApJ, 873, L1

—. 2021a, ApJ, 914, 98

—. 2021b, ApJ, 914, 99

Wang, L., & Goodman, J. 2017, ApJ, 847, 11

Wang, S., Wang, L., & Dong, S. 2025, ApJS, 276, 40

Yang, H., & Wang, L. 2025, arXiv e-prints, arXiv:2512.01283

Yao, J., Yi, Y., Hang, L., et al. 2025, Solving Multiscale Dynamical Systems by Deep Learning, arXiv, arXiv:2401.01220

Yue, N., Wang, L., Bisbas, T., Quan, D., & Li, D. 2024, ApJ, 973, 37

Zhang, X., Yi, Y., Wang, L., et al. 2025, ApJ, 990, 105

Zingale, M., Bhargava, K., Brady, R., et al. 2024, arXiv e-prints, arXiv:2411.12491